Alternative fast quantum logic gates using nonadiabatic Landau-Zener-Stückelberg-Majorana transitions

A. I. Ryzhov [1,2] O. V. Ivakhnenko [1,2] S. N. Shevchenko [1] M. F. Gonzalez-Zalba [3] and Franco Nori [2,4,5]

[1]*B. Verkin Institute for Low Temperature Physics and Engineering, Kharkiv 61103, Ukraine*
[2]*Theoretical Quantum Physics Laboratory, Cluster for Pioneering Research, RIKEN, Wakoshi, Saitama 351-0198, Japan*
[3]*Quantum Motion, 9 Sterling Way, London N7 9HJ, United Kingdom*
[4]*Quantum Computing Center, RIKEN, Wakoshi, Saitama 351-0198, Japan*
[5]*Physics Department, The University of Michigan, Ann Arbor, Michigan 48109-1040, USA*

A conventional realization of quantum logic gates and control is based on resonant Rabi oscillations of the occupation probability of the system. This approach has certain limitations and complications, like counter-rotating terms. We study an alternative paradigm for implementing quantum logic gates based on Landau-Zener-Stückelberg-Majorana (LZSM) interferometry with nonresonant driving and the alternation of adiabatic evolution and nonadiabatic transitions. Compared to Rabi oscillations, the main differences are a nonresonant driving frequency and a small number of periods in the external driving. We explore the dynamics of a multilevel quantum system under LZSM drives and optimize the parameters for increasing the gate speed. We define the parameters of the external driving required for implementing a specific quantum logic gate using the adiabatic-impulse model. In particular, we demonstrate the implementations of single-qubit X, Y, Hadamard gates, and two-qubit iSWAP and CNOT gates using the LZSM transitions. The considered LZSM approach for implementing arbitrary quantum logic gates can be applied to a large variety of multilevel quantum systems and external driving.

I. INTRODUCTION

The conventional way of qubit state control is realized with resonant driving, resulting in Rabi oscillations (see, e.g., Refs. [1–4]). There, the Rabi frequency is determined by the driving amplitude; thus increasing the driving amplitude increases the speed of operation. This presents several challenges [5,6], including leakage to levels that lie outside the qubit subspace, breakdown of the rotating-wave approximation, and increased environmental noise. Instead of discussing the technological complications of the Rabi approach, let us consider here an alternative approach, based on a different paradigm of driving quantum systems.

When a quantum system exhibits an avoided-level crossing and is strongly driven, it can be described by the model originally developed in several publications in 1932 and known as Landau-Zener-Stückelbeg-Majorana (LZSM) transitions (see, e.g., Refs. [7–12] and references therein). Effectively, the model can be split into two evolution stages: nonadiabatic transitions between the energy levels in the vicinity of the anticrossing and adiabatic evolution far from the anticrossing.

The energy-level occupation probabilities, as well as the relative phase between them, can be chosen by varying the driving parameters (the driving frequency and amplitude), providing a different paradigm for qubit state control [8,13].

LZSM transitions provide an alternative to conventional gates based on resonant driving [14,15]. The avoided energy level crossing of a single qubit or two coupled qubits allows to controllably change states of such systems [16–19] and to realize single- and two-qubit logic operations [6]. Recently, it was studied theoretically [20–23] and demonstrated experimentally [6,24–30] that the LZSM model has several advantages over conventional gates based on Rabi oscillations. These advantages include ultrafast speed of operation [24,31], robustness [21], using baseband pulses (alleviating the need for pulsed-microwave control signals) [6], and reducing the effect of environmental noise [26].

In this work, we further develop the paradigm of LZSM-based quantum logic gates. We investigate the single- and two-qubit systems' dynamics under an external drive by numerically solving the Liouville-von Neumann equation using the QuTiP [32,33]. We explore ways of finding the parameters for any arbitrary quantum logic gate with LZSM transitions and optimize the composition of the speed and fidelity of the quantum logic gates. We demonstrate the implementation of single-qubit X, Y, Hadamard gates, and two-qubit iSWAP and CNOT gates using LZSM transitions.

This paper is organized as follows. In Sec. II, we describe the qubit Hamiltonian and its two main bases. In Sec. III, we demonstrate the X, Y, Hadamard, and phase gates implementations using both Rabi oscillations and LZSM transitions. We compare the speed and fidelities achieved with both

paradigms. We explore the way of increasing the gate speed and fidelity of the LZSM gates by using multiple transitions. In Sec. IV, we generalize the considered paradigm of using the adiabatic-impulse model to realize quantum logic gates for multilevel quantum systems, and describe the realization of a two-qubit iSWAP gate with two LZSM transitions. The details for implementing other two-qubit gates, in particular a CNOT gate, are provided in Appendices A and B. Section V presents the conclusions.

II. HAMILTONIAN AND BASES

Consider the typical Hamiltonian for a driven quantum two-level system

$$H(t) = \frac{\Delta}{2}\sigma_x + \frac{\varepsilon(t)}{2}\sigma_z = \frac{1}{2}\begin{pmatrix} \varepsilon(t) & \Delta \\ \Delta & -\varepsilon(t) \end{pmatrix}, \quad (1)$$

where $\varepsilon(t)$ is the driving signal and Δ is the minimal energy gap between the two levels. Here we consider the harmonic driving signal

$$\varepsilon(t) = A \sin \omega t. \quad (2)$$

The wave function is a superposition of two states of a quantum two-level system:

$$|\psi\rangle = \alpha(t)|0\rangle + \beta(t)|1\rangle = \begin{pmatrix} \alpha(t) \\ \beta(t) \end{pmatrix}. \quad (3)$$

The two main bases are: the *diabatic* one, with diabatic energy levels $\{|0\rangle, |1\rangle\}$, where the Hamiltonian becomes diagonalized when $\Delta = 0$, and the *adiabatic* basis $|E_\pm\rangle$, representing the eigenvalues of the total Hamiltonian, see Fig. 1. The relation between these bases is given by

$$|E_\pm(t)\rangle = \gamma_\mp |0\rangle \mp \gamma_\pm |1\rangle, \quad (4a)$$

where

$$\gamma_\pm = \frac{1}{\sqrt{2}}\sqrt{1 \pm \frac{\varepsilon(t)}{\Delta E(t)}}. \quad (4b)$$

Hereafter, all the matrices of quantum logic gates, rotations $R_{x,y,z}$, matrices of adiabatic evolution U, and diabatic transition N are represented in the adiabatic basis; while the Hamiltonians are represented in the diabatic one. Specifically, in Secs. II and III, the Hamiltonian of a single qubit is defined in the diabatic basis $\{|1\rangle, |0\rangle\}$, and the matrices are represented in the adiabatic basis $\{|E_+\rangle, |E_-\rangle\}$ with the energies in descending order. In Sec. IV, Appendices A and B, the Hamiltonian of two qubits is defined in the diabatic basis $\{|00\rangle, |01\rangle, |10\rangle, |11\rangle\}$, and the matrices are represented in the adiabatic basis $\{|E_0\rangle, |E_1\rangle, |E_2\rangle, |E_3\rangle\}$ with the energies in ascending order. The order of the basis vectors is important, as it determines the matrix representation of a given operator in this basis.

The dynamics of the quantum system with relaxation and dephasing can be described by the Lindblad equation. For simplicity, we consider the dynamics without relaxation and dephasing, described by the Liouville-von Neumann equation

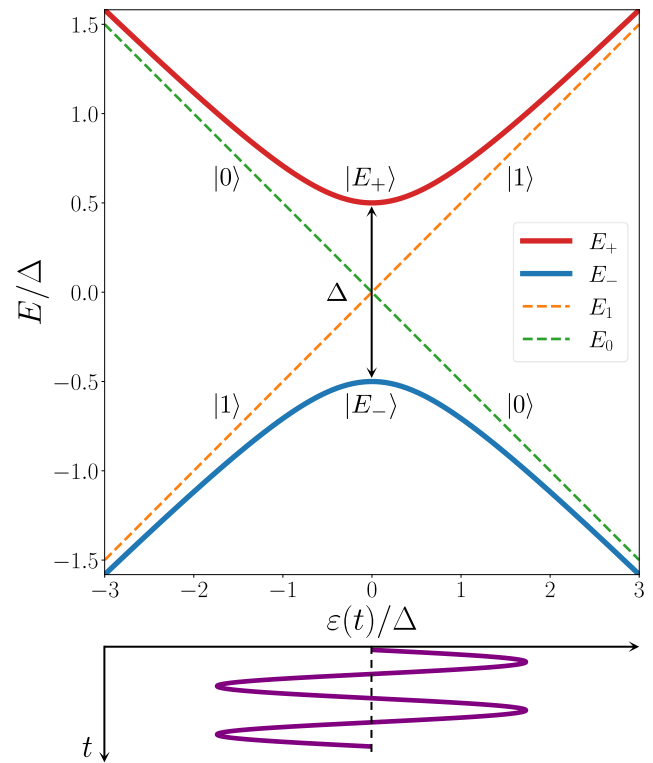$$\frac{d\rho}{dt} = -\frac{i}{\hbar}[H(t), \rho], \quad (5)$$

FIG. 1. Energy diagram of a quantum two-level system under a periodic drive $\varepsilon(t)$. Energy levels structure with two crossed diabatic levels $|0\rangle$, $|1\rangle$ and two adiabatic levels $|E_\pm\rangle$ with the an avoided crossing as a function of an energy detuning $\varepsilon(t)$.

which coincides with the Bloch equations in the case of a two-level system.

III. SINGLE-QUBIT GATES

We will describe a basic set of single-qubit gates (Sec. III A) and then explain how these can be performed using both the Rabi approach (Sec. III B) and the LZSM approach (Sec. III C).

A. Basic set of single-qubit gates. Phase gate $R_z(\phi)$

We consider different gates [34]: X, Y, Z gates, phase gate $R_z(\phi)$, and the Hadamard gate H; which we write down here:

$$X = \sigma_x = R_x(\pi) = \begin{pmatrix} 0 & 1 \\ 1 & 0 \end{pmatrix}, \quad (6)$$

$$Y = \sigma_y = R_y(\pi) = \begin{pmatrix} 0 & -i \\ i & 0 \end{pmatrix} \Leftrightarrow R_z(\pi)R_x(\pi), \quad (7)$$

$$Z = \sigma_z = R_z(\pi) = \begin{pmatrix} 1 & 0 \\ 0 & -1 \end{pmatrix}, \quad (8)$$

$$P(\phi) \equiv R_z(\phi) = \begin{pmatrix} 1 & 0 \\ 0 & e^{i\phi} \end{pmatrix} \Leftrightarrow \begin{pmatrix} e^{-i\phi/2} & 0 \\ 0 & e^{i\phi/2} \end{pmatrix}, \quad (9)$$

$$H = R_y(\pi/2)R_z(\pi) = \sqrt{Y}Z = \frac{1}{\sqrt{2}}\begin{pmatrix} 1 & 1 \\ 1 & -1 \end{pmatrix}, \quad (10)$$

where $R_{x,y,z}$ describes the rotations around the respective axes:

$$R_{x,y,z}(\phi) = \exp\left(-i\sigma_{x,y,z}\frac{\phi}{2}\right)$$

$$= \cos\left(\frac{\phi}{2}\right)I + i\sin\left(\frac{\phi}{2}\right)X, Y, Z. \quad (11)$$

Since the global phase of the density matrix ρ is irrelevant and the dynamics is invariant to the multiplication of the density matrix ρ by any complex number from the unit circle $e^{i\varphi}$, the gate operator $e^{i\varphi}G$ is equivalent to the gate operator G, which we denote as

$$e^{i\varphi}G \Leftrightarrow G. \quad (12)$$

The first gate we consider is the phase gate $R_z(\phi)$ in Eq. (9), which corresponds to a rotation around the z axis by an angle ϕ. Similarly to a spin rotating in a magnetic field (the Larmor precession with frequency Ω_L), there is a free natural rotation of the Bloch vector around the z axis. The frequency of this free rotation is proportional to the distance between the energy levels

$$\hbar\Omega_L = \Delta E = \sqrt{\varepsilon(t)^2 + \Delta^2}. \quad (13)$$

After a period of time

$$t_{R_z}(\phi) = \frac{\phi}{\Omega_L}. \quad (14)$$

the Bloch vector rotates by an angle ϕ, and effectively the qubit performs the phase gate $R_z(\phi)$. There is no need of a drive to perform this gate: $\varepsilon = $ const.

In the Rabi-based approach, the energy detuning of the qubit during the phase gate is at the level anticrossing $\varepsilon = 0$. While in the LZSM-based approach, it can be far away from the anticrossing. Therefore the time of the phase gate in the LZSM-based approach can be reduced. This difference in duration of the phase gates is demonstrated in Figs. 2(a) and 3(a).

B. Rabi-based single-qubit gates

1. Rectangular-shaped pulses

To perform any quantum logic gate with changing level occupation probability, the qubit should be excited by a time-dependent energy detuning $\varepsilon(t)$. A conventional way to achieve this is via Rabi oscillations with small amplitude $A \ll \Delta$ and with the qubit resonant frequency ($\hbar\omega = \Delta$), which we will compare to LZSM transitions with large amplitude $A > \Delta$ and nonresonant driving frequency ω.

Here we describe how the single-qubit operations are implemented with Rabi oscillations and demonstrate the dynamics of the Bloch sphere coordinates for several logic gates in Fig. 2. Rabi oscillations occur during the resonant driving at $\delta\omega = \omega - \omega_q \ll \omega$ (where $\omega_q = \Delta E/\hbar \approx \Delta/\hbar$ is the qubit resonant frequency) with small amplitude $A \ll \Delta$, and harmonic driving signal, Eq. (2).

The Rabi oscillations lead to a periodic change of the level occupation with Rabi frequency

$$\Omega_R = \frac{A\Delta}{2\hbar\Delta E} \approx \frac{A}{2\hbar}. \quad (15)$$

Note that this differs from the common value for the Rabi frequency $\Omega_R \approx A/\hbar$ (see Refs. [7,35]). During the oscillations, the z component of the Bloch vector changes as $z(t) = \cos\Omega_R t$, when the initial state is the ground state $|E_-\rangle$. While the state probability is evolving, a phase change also occurs with frequency

$$\hbar\Omega_L \approx \Delta. \quad (16)$$

We define the Rabi oscillations evolution as a combination of two rotations

$$U_{\text{Rabi}}(t) = R_z(\Omega_L t)R_x(\Omega_R t). \quad (17)$$

Using Eq. (15), we can rewrite it as

$$U_{\text{Rabi}}(t) = R_z(\Omega_L t)R_x\left(\frac{A}{2\hbar}t\right) = R_z(\Omega_L t)R_x\left(\frac{S}{2\hbar}\right), \quad (18)$$

which shows that the angle of rotation around the x-axis is proportional to the area $S = At$ under the envelope of the Rabi pulse.

When there is no phase difference between rotations, $\Omega_L t = \Omega_R t + 2\pi n$, we obtain

$$U_{\text{Rabi}}(t) = R_z(\Omega_L t)R_x(\Omega_R t) = R_y(\Omega_R t), \quad (19)$$

and the Rabi evolution results in a rotation around the y axis.

To perform an X operation, we drive the system by Rabi pulses during a time T_R, so that the area under the envelope is

$$S = AT_R = 2\pi\hbar. \quad (20)$$

In order for the driving to end at zero amplitude, we take an integer number of periods of the sine.

After that, we need to change the phase to obtain an X operation from a Y rotation, so we perform the R_z rotation by idling the drive for a time T_I with the condition

$$\Omega_L(T_I + T_R) = 2\pi n, \quad (21)$$

then finally the X gate is realized as

$$R_z(\Omega_L T_I)U_{\text{Rabi}}(T_R) = R_z(\Omega_L T_I)R_z(\Omega_L T_R)R_x(\Omega_R T_R)$$
$$= R_x(\pi) = X, \quad (22)$$

see Fig. 2(c). To perform the Hadamard gate, we need to apply the Rabi pulse with its duration twice shorter than for the X gate, $T_R = \pi/\Omega_R$, with the condition on the idling time T_I:

$$\Omega_L(T_I + T_R) = \pi + 2\pi n. \quad (23)$$

As a result, we obtain the Hadamard gate as

$$R_z(\Omega_L T_I)U_{\text{Rabi}}(T_R) = R_z(\Omega_L T_I)R_z(\Omega_L T_R)R_x(\Omega_R T_R)$$
$$= R_z(\pi)R_x(\pi/2) = H, \quad (24)$$

which is shown in Fig. 2(b).

2. Gaussian-shaped optimized pulses

Since the Rabi-oscillations model assumes small amplitudes of the driving signal, to increase the gate fidelity, a small amplitude at the start and end points should be used. To achieve a high gate speed, a large driving amplitude A between these points should be used. Hence, to increase the gate speed,
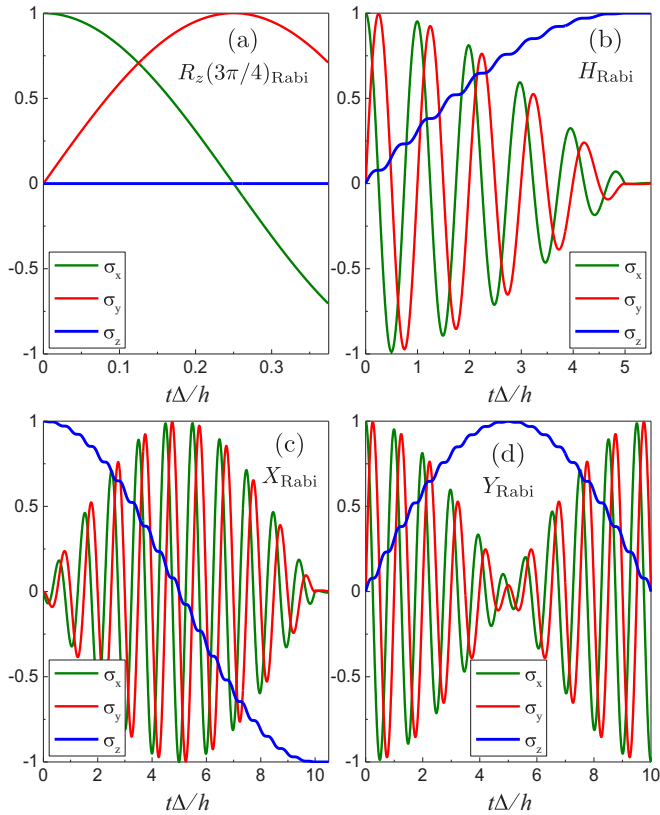
FIG. 2. Rabi-based single-qubit operations. Dynamics of the Bloch vector components in the adiabatic basis, obtained by solving the Liouville-von Neumann Eq. (5). (a) Phase operation $R_z(3\pi/4)$ with the superposition initial state $\psi(t=0) = (|E_-\rangle + |E_+\rangle)/\sqrt{2}$. (b) Hadamard operation H with the same superposition initial state. (c) X operation with the ground-state initial conditions. (d) Y operation with the superposition initial state. For (b)–(d), the driving frequency is resonant $\hbar\omega = \Delta$, the amplitude is small $A = 0.1\Delta$. For (b), the number of periods of the resonant drive is $N_e = 5$, for (c) and (d) $N_e = 10$. Here, the amplitude is defined by the number of periods of the external drive, for (b) $A = \Delta/2N_e$, for (c) and (d) $A = \Delta/N_e$.
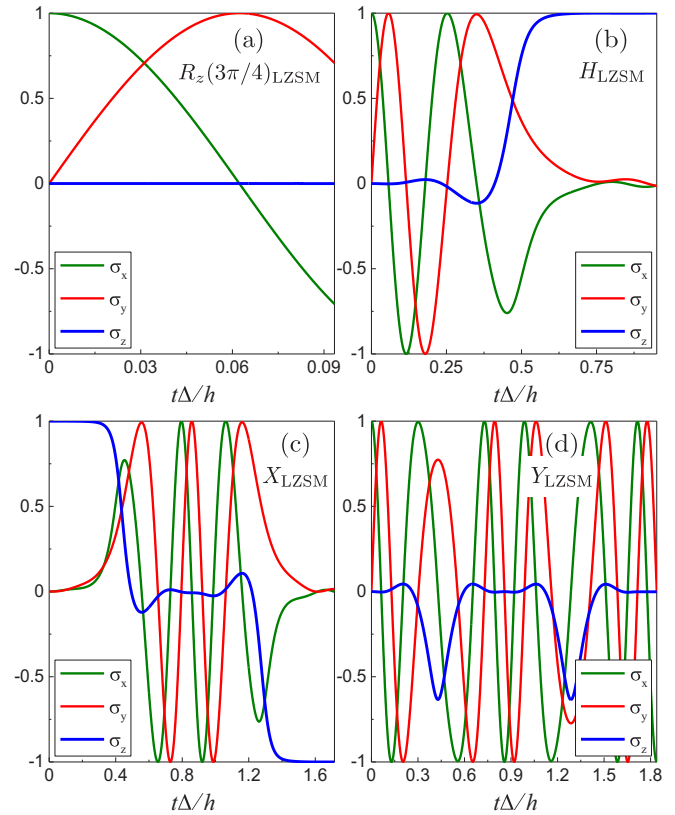
FIG. 3. LZSM-based single-qubit operations. Dynamics of the Bloch vector components in the adiabatic basis, obtained by solving the Liouville-von Neumann Eq. (5). (a) Phase operation $R_z(3\pi/4)$ with the superposition initial state $\psi(t=0) = (|E_-\rangle + |E_+\rangle)/\sqrt{2}$ and the energy detuning $\varepsilon = 3.8872\Delta$. (b) Hadamard operation H with superposition initial state. (c) X operation with ground-state initial conditions. (d) Y operation with the superposition initial state. For (b)–(d), the parameters are chosen so that $\mathcal{P} = 0.5$. For (b), the amplitude $A = 4.31\Delta$, for (c) and (d) $A = 3.8872\Delta$. Compared with the respective gates based on Rabi oscillations, Fig. 2, the LZSM-based gates are much faster.

now we use a Gaussian-shaped envelope $A(t)$ for the driving signal

$$\varepsilon(t) = A(t)\sin\omega t. \tag{25}$$

We now consider a Rabi pulse with duration T_R and envelope in the form

$$A(t) = \begin{cases} A_0 \exp\left[-\frac{(t-\tau)^2}{2\sigma_G^2}\right], & t < T_R \\ 0, & t > T_R \end{cases} \tag{26}$$

with the tails of the Gaussian distribution truncated at some distance G from the peak, normalized to the standard deviation σ_G,

$$G = \frac{T_R}{2\sigma_G} \tag{27}$$

and the peak of the distribution at time

$$\tau = \frac{T_R}{2}. \tag{28}$$

The angle of rotation around the x axis in Eq. (18) is determined by the area under the envelope of the Rabi pulse. For the X operation it is given by Eq. (20). So the area under the truncated Gaussian distribution should be the same as for the original signal with constant amplitude and rectangular shape of the pulse. This condition determines the amplitude of the distribution as

$$A_0 = \sqrt{\frac{2\pi}{\sigma_G S_G}}, \tag{29}$$

where S_G is the normalized area of the truncated Gaussian distribution

$$S_G = \frac{1}{\sqrt{2\pi}} \int_{-G}^{G} e^{-\frac{x^2}{2}} dx. \tag{30}$$

C. Single-qubit gates based on LZSM transitions

Here we describe how to implement single-qubit operations based on LZSM transitions using the adiabatic-impulse model (AIM), also known as the transfer-matrix method. We

demonstrate the dynamics of the Bloch sphere coordinates for several logic gates in Fig. 3, that can be compared with the dynamics of the same gates realized with Rabi oscillations in Fig. 2. For the diabatic LZSM transitions, we need the following approximations: $A > \Delta$ and $2\pi/\omega < t_{\text{trans}}$, where t_{trans} is the transition time. After that time, the result of the adiabatic-impulse model will asymptotically coincide with the exact dynamics [8,36].

1. Adiabatic-impulse model. Single-passage drive

In the adiabatic-impulse model, the time evolution is considered as a combination of adiabatic (nontransition) and diabatic (transition) evolutions. The *adiabatic* evolution is described by the adiabatic time-evolution operator, which in the adiabatic basis $\{|E_+\rangle, |E_-\rangle\}$ is represented by the matrix

$$U(t_i, t_j) = \begin{pmatrix} e^{-i\zeta(t_i,t_j)} & 0 \\ 0 & e^{i\zeta(t_i,t_j)} \end{pmatrix} = e^{-i\zeta\sigma_z} = R_z(2\zeta), \quad (31)$$

where $\zeta(t_i, t_j)$ is the phase accumulated during the adiabatic evolution

$$\zeta(t_i, t_j) = \frac{1}{2\hbar} \int_{t_i}^{t_j} \Delta E(t) \, dt = \frac{1}{2\hbar} \int_{t_i}^{t_j} \sqrt{\varepsilon(t)^2 + \Delta^2} dt, \quad (32)$$

and $\Delta E(t) = E_+(t) - E_-(t)$. Then, the *diabatic* evolution (transition) operator for a passage in the direction of the energy detuning $\varepsilon(t)$ increase is represented by the matrix

$$N = \begin{pmatrix} Re^{-i\phi_S} & -T \\ T & Re^{i\phi_S} \end{pmatrix} = R_z(\phi_S)R_x(\theta)R_z(\phi_S), \quad (33)$$

where

$$T = \sqrt{\mathcal{P}}, \quad R = \sqrt{1 - \mathcal{P}} \quad (34)$$

are the transition and reflection coefficients,

$$\mathcal{P} = \exp(-2\pi\delta) \quad (35)$$

is the LZSM probability of excitation of the qubit with a single transition from the ground state $|E_-\rangle$, $\delta = \Delta^2/4v$ is the adiabaticity parameter, $v = \varepsilon'(0)$ is the speed of the anticrossing passage and

$$\phi_S = \frac{\pi}{4} + \delta(\ln\delta - 1) + \text{Arg}[\Gamma(1 - i\delta)] \quad (36)$$

is the Stokes phase [8]. The θ angle can be found from the equation

$$\sin^2(\theta/2) = \mathcal{P}. \quad (37)$$

The transition matrix for a passage when the energy detuning $\varepsilon(t)$ decreases, which we denote as the *inverse* transition matrix, can be written as

$$N^{\text{inv}} = N^\top = \begin{pmatrix} Re^{-i\phi_S} & T \\ -T & Re^{i\phi_S} \end{pmatrix} \Leftrightarrow \begin{pmatrix} Re^{-i(\phi_S - \pi)} & -T \\ T & Re^{i(\phi_S - \pi)} \end{pmatrix}. \quad (38)$$

The single transition evolution matrix in the general case with *adiabatic* evolution matrix before the transition U_1 and after the transition U_2 is given by

$$U_{\text{LZSM}} = U_2 N_1 U_1 = \begin{pmatrix} U'_{11} & U'_{12} \\ -U'^*_{12} & U'^*_{11} \end{pmatrix}, \quad (39)$$

where

$$U'_{11} = R_1 \exp[-i(\phi_{S1} + \zeta_1 + \zeta_2)],$$
$$U'_{12} = -T_1 \exp[i(\zeta_1 - \zeta_2)],$$
$$\zeta_1 = \zeta(0, t_{N1}),$$
$$\zeta_2 = \zeta(t_{N1}, t_{\text{final}}).$$

Here, t_{N1} is the time of the level anticrossing passage, t_{final} is the end time of the drive.

Then, we consider the same adiabatic evolution before and after the transition $\zeta = 2\zeta_1 = 2\zeta_2$. In that case, a single LZSM transition gate can be represented [37,38] as a combination of rotations

$$U_{\text{LZSM}}(\mathcal{P}, \phi_{\text{total}}) = R_z(\phi_{\text{total}})R_x(\theta)R_z(\phi_{\text{total}}),$$
$$U_{\text{LZSM}}^{\text{inv}}(\mathcal{P}, \phi_{\text{total}}) = U_{\text{LZSM}}(\mathcal{P}, \phi_{\text{total}} - \pi), \quad (40)$$

where $\phi_{\text{total}} = \phi_S + \zeta$, and $U_{\text{LZSM}}^{\text{inv}}$ corresponds to the inverse transition. Using this LZSM gate, we can define a basic set of gates.

For an X gate, the two-level system needs to perform a transition with probability $\mathcal{P} = \exp(-2\pi\delta) = 1$; which means that the adiabaticity parameter $\delta = \Delta^2/4v \to 0$, requiring an infinite speed of the anticrossing passage $v = \varepsilon'(0) \to \infty$ or a zero energy splitting Δ. Hence, it is difficult to implement the X operation with high fidelity using only a single passage. Therefore at least two transitions are needed for implementing the X gate with sufficient fidelity.

For the LZSM transition, we need to start and finish the evolution far from the anticrossing region. So we now consider the harmonic driving signal $\varepsilon(t) = -A\cos\omega t$, $t \in [0, \pi/\omega]$. This signal is linear in the anticrossing region

$$\frac{d\varepsilon}{dt}\bigg|_{\varepsilon \approx 0} \approx A\omega = \text{const.} \quad (41)$$

We obtain a relation between the amplitude A and the frequency ω for certain LZSM probability $\mathcal{P}$

$$\mathcal{P} = \exp\left[-2\pi\frac{\Delta^2}{4A\omega\hbar}\right] \to \omega = \frac{-\pi\Delta^2}{2A\hbar\ln\mathcal{P}}. \quad (42)$$

Then, we find an amplitude which satisfies some values of ϕ_{total} and $\mathcal{P}$,

$$\phi_{\text{total}} = \frac{\pi}{4} + \delta(\ln\delta - 1) + \text{Arg}[\Gamma(1 - i\delta)]$$
$$+ \frac{1}{2\hbar}\int_0^{\frac{\pi}{\omega}} \sqrt{\varepsilon(t)^2 + \Delta^2} dt, \quad (43)$$

$$\delta = -\frac{\ln\mathcal{P}}{2\pi}, \quad (44)$$

where we used that the harmonic driving satisfies the initial conditions far from the anticrossing region.

A single LZSM transition is convenient for implementing rotations to any angle $\theta < \pi$, for example $\theta = \pi/2$, which is needed for the Hadamard gate. Following Eq. (37), the angle $\theta = \pi/2$ corresponds to the target probability of a single LZSM transition

$$\mathcal{P} = \sin^2\left(\frac{\pi}{4}\right) = \frac{1}{2}. \quad (45)$$

This LZSM transition is *noninstantaneous*: the probability oscillates for some time after the transition, and the value of the upper-level occupation obtained from the formulas cannot be exactly reached until the end of the oscillations [36]. The parameters for the Hadamard gate implementation can be found from Eq. (39) by equating U_{LZSM} to the matrix of the gate (10), and solving the system of equations

$$\mathcal{P} = \frac{1}{2} \rightarrow T = R = \frac{1}{\sqrt{2}},$$

$$\zeta_1 - \zeta_2 = \frac{\pi}{2} + \pi n_1,$$

$$\phi_S + \zeta_1 + \zeta_2 = \frac{\pi}{2} + \pi n_2. \tag{46}$$

From this system, we obtain the total phase

$$\phi_{\text{total}} = \pi n, \tag{47}$$

so the Hadamard gate can be presented as

$$H = R_y(\pi/2)R_z(\pi) = U_{\text{LZSM}}(1/2, 2\pi n)R_z(\pi)$$
$$= R_z(\pi)U_{\text{LZSM}}(1/2, \pi + 2\pi n), \tag{48}$$

where n is an integer. The dynamics of the Hadamard gate is shown in Fig. 3(b).

How to find the driving amplitude A and frequency ω required for certain $\mathcal{P}$ and ϕ_{total} is described in Sec. III C 3. After the transition is completed, to perform some rotation around the z axis (phase gate), we need to apply a constant signal with the same energy detuning ε as we had after completing the previous operation.

Alternatively, LZSM gates can also be realized with the position of the energy detuning before and after the gate at the level anticrossing $\varepsilon = 0$ [6].

2. Double-passage drive

Consider now an arbitrary external drive $\varepsilon(t)$ with two passages through the energy-level anticrossing, linear in the anticrossing region. The adiabatic energy levels as a function of time are illustrated in Fig. 4(a).

We obtain the double transition evolution matrix in the general case:

$$\Xi = U_3 N_2 U_2 N_1^{\text{inv}} U_1 = U_{\text{LZSM}(1)}^{\text{inv}} U_{\text{LZSM}(2)} = \begin{pmatrix} \Xi_{11} & \Xi_{12} \\ -\Xi_{12}^* & \Xi_{11}^* \end{pmatrix}, \tag{49}$$

where

$$\Xi_{11} = (R_1 R_2 e^{-i(\phi_{S1}+\phi_{S2}+2\zeta_2)} + T_1 T_2)e^{i(\zeta_2-\zeta_1-\zeta_3)},$$

$$\Xi_{12} = (R_1 T_2 - T_1 R_2 e^{-i(\phi_{S1}+\phi_{S2}+2\zeta_2)})e^{i(\phi_{S1}+\zeta_1+\zeta_2-\zeta_3)},$$

$$\zeta_1 = \zeta(0, t_{N1}),$$

$$\zeta_2 = \zeta(t_{N1}, t_{N2}),$$

$$\zeta_3 = \zeta(t_{N2}, t_{\text{final}}).$$

Here, t_{N1} and t_{N2} are the times of the first and second passages of the level anticrossing respectively, t_{final} is the end time of the drive, see Fig. 4.

By equating this evolution matrix to the matrix of the required quantum gate, one can find the parameters of the
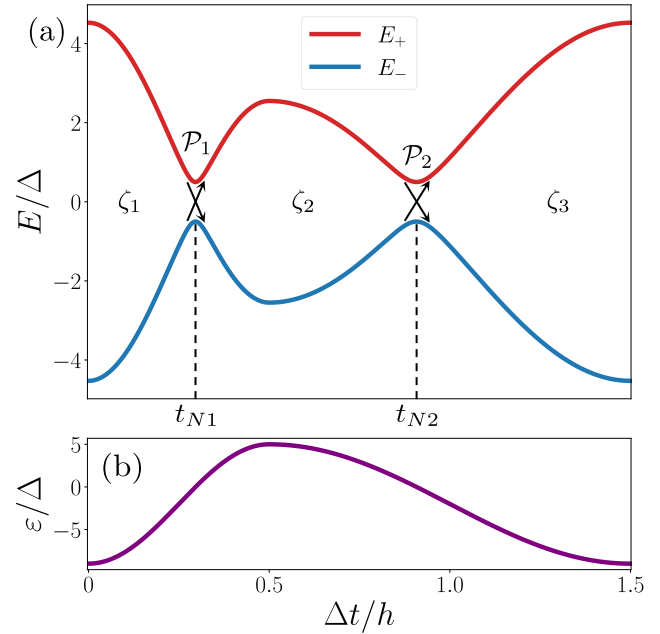

FIG. 4. Energy levels dynamics for a drive with two passages of the level anticrossing. (a) Adiabatic energy levels versus time. (b) The energy detuning ε versus time. Here, $\mathcal{P}_i$ is the value of the LZSM probability of the diabatic transition N_i during the passage of the level anticrossing at time $t_{N(i)}$. Here, ζ_i is the phase accumulation gained during the corresponding adiabatic evolution interval.

driving signal that implements this gate. For example, for an X gate, the driving signal should satisfy the conditions

$$\mathcal{P}_1 + \mathcal{P}_2 = 1 \rightarrow T_1 = R_2,$$

$$\phi_{S1} + \phi_{S2} + 2\zeta_2 = \pi + 2\pi n_1,$$

$$\phi_{S2} - \zeta_1 + \zeta_2 + \zeta_3 = \pi/2 + 2\pi n_2. \tag{50}$$

To simplify the result, we consider a periodic driving with the same slope in the anticrossing region during each transition $\varepsilon(0) \approx vt$, which means $\mathcal{P}_1 = \mathcal{P}_2 = 1/2$, $T_1 = T_2 = R_1 = R_2 = 1/\sqrt{2}$, and with the same adiabatic evolution between transitions $\zeta = \zeta_1 = \zeta_2/2 = \zeta_3$. After this simplification, we obtain a matrix of the double transitions with only two parameters [8]: adiabatic phase gain ζ and excitation probability $\mathcal{P}$, with

$$\Xi \equiv \sqrt{U_2} N^{\text{inv}} U_1 N \sqrt{U_2} = \begin{pmatrix} \Xi_{11} & \Xi_{12} \\ -\Xi_{12}^* & \Xi_{11}^* \end{pmatrix}, \tag{51a}$$

where

$$\Xi_{11} = -R^2 e^{-2i\Phi_{St}} - T^2, \tag{51b}$$

$$\Xi_{12} = -\Xi_{12}^* = -2iRT \sin(\Phi_{St}), \tag{51c}$$

$$\Phi_{St} \equiv \phi_S + \zeta, \tag{51d}$$

and Φ_{St} is a Stückelberg phase. For the symmetric drive with $\mathcal{P}_1 = \mathcal{P}_2$ and $\zeta = \zeta_1 = \zeta_2/2 = \zeta_3$, $\Phi_{St} = \phi_{\text{total}}$. For the X operation, shown in Fig. 3(c), we used the drive $\varepsilon(t) = -A \cos \omega t$, $t \in [0, 2\pi/\omega]$ with two LZSM transitions with LZSM probability $\mathcal{P} = 1/2$, and total phase for each

transition

$$\phi_{\text{total}} = \frac{\pi}{2} + \pi n, \qquad (52)$$

which is the condition for a constructive interference (see, e.g., Ref. [8]). Indeed, using Eq. (40),

$$U_{\text{LZSM}}^{\text{inv}}(\pi/2 + \pi n, 1/2)U_{\text{LZSM}}(\pi/2 + \pi n, 1/2) = R_x(\pi) = X. \qquad (53)$$

In principle, a double LZSM transition drive, in conjunction with a rotation around the z axis, can implement any single-qubit gate.

For the Hadamard gate implemented by two LZSM transitions with the same slope in the anticrossing region during each transition ($\mathcal{P}_1 = \mathcal{P}_2$), the driving signal should satisfy the conditions

$$\mathcal{P} = \frac{2 \pm \sqrt{2}}{4},$$

$$\phi_S + \zeta_2 = \frac{\pi}{2} + 2\pi n_1,$$

$$\zeta_1 + \zeta_2 + \zeta_3 = \frac{\pi}{2} + 2\pi n_2,$$

$$\zeta_1 - \zeta_3 = 2\pi n_3. \qquad (54)$$

3. Optimization to speed up gates: multiple passage drive

To speed up the gate, multiple LZSM transitions can be used. We consider the simplest drive

$$\varepsilon(t) = \begin{cases} -A, & 0 < t < t_{\text{pre}}, \\ -A\cos\omega t, & t_{\text{pre}} < t < t_{\text{pre}} + \frac{2\pi k}{\omega}, \\ -A, & t_{\text{pre}} + \frac{2\pi k}{\omega} < t < t_{\text{pre}} + \frac{2\pi k}{\omega} + t_{\text{after}}, \end{cases} \qquad (55)$$

with an even number $2k$ of successive LZSM transitions with the same probability of LZSM transition $\mathcal{P}$, and Stückelberg phase Φ_{St}, and the idling periods with phase accumulation at the start and end of the drive with durations t_{pre} and t_{after}, respectively. Here, $k = 1, 2, \ldots$ is the number of periods of the cosine.

For the case of four LZSM transitions, the evolution matrix of the harmonic part of the drive, $\varepsilon(t) = -A\cos\omega t$, can be found as the multiplication of two evolution matrices for double passage (51):

$$\Xi_Q = \Xi^2 = \begin{pmatrix} \Xi_{Q11} & \Xi_{Q12} \\ -\Xi_{Q12}^* & \Xi_{Q11}^* \end{pmatrix}, \qquad (56a)$$

where

$$\Xi_{Q11} = R^4 e^{-4i\Phi_{\text{St}}} + T^4 + 2R^2T^2[e^{-2i\Phi_{\text{St}}} - 2\sin^2(\Phi_{\text{St}})], \qquad (56b)$$

$$\Xi_{Q12} = 4iRT\sin(\Phi_{\text{St}})[R^2\cos(2\Phi_{\text{St}}) + T^2]. \qquad (56c)$$

Since $T = \sqrt{\mathcal{P}}$ and $R = \sqrt{1 - \mathcal{P}}$, the evolution matrix depends on two parameters of the drive: the probability of a single LZSM transitions $\mathcal{P}$, and the Stückelberg phase Φ_{St}. The idling periods before and after the main part of the drive result in the phase-shift gates $R_z(\phi_{\text{pre}})$ and $R_z(\phi_{\text{after}})$, respectively [see Eq. (9)].
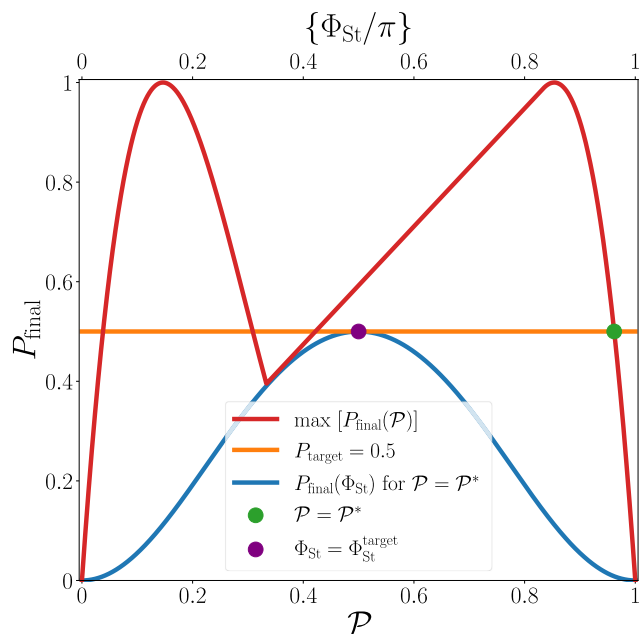

FIG. 5. Graphical demonstration of finding the values of a single LZSM transition probability $\mathcal{P}$ and Stückelberg phase Φ_{St}, for the implementation of the Hadamard gate H with four LZSM transitions. Red curve: maximum possible final occupation probability after four transitions P_{final} depending on $\mathcal{P}$. Blue curve: dependence of the final occupation probability after four transitions P_{final} on the Stückelberg phase gain during single-transition Φ_{St}. The orange horizontal line shows $P_{\text{final}} = P_{\text{target}}$.

The parameters of the drive are found by equating the total evolution matrix of the driven qubit to the matrix of the required operation, multiplied by the factor $e^{i\varphi}$ with an arbitrary φ, as it does not affect the dynamics of the system [see Eq. (12)]:

$$R_z(\phi_{\text{pre}})\Xi_Q R_z(\phi_{\text{after}}) = e^{i\varphi}H. \qquad (57)$$

Here we describe an *algorithm for finding the optimal parameters* ($\mathcal{P}$, Φ_{St}, A, ω, t_{pre}, t_{after}) *of the drive* with four LZSM transitions that implements the Hadamard gate H.

The occupation probability of the excited state of the qubit $|E_+\rangle$ after applying the drive with four LZSM transitions to the qubit in the ground state $|E_-\rangle$ is given by

$$P_{\text{final}} = |\Xi_{Q12}|^2. \qquad (58)$$

(1) First, we find the possible values of a single LZSM transition probability $\mathcal{P}$ that provide the target final upper energy-level occupation probability after four transitions $P_{\text{final}} = P_{\text{target}}$. These can be found as the crossings of the red curve and orange horizontal line in Fig. 5. The red curve shows the maximum possible final upper energy-level occupation after four LZSM transitions P_{final}, after varying through all possible values of $\Phi_{\text{St}} \in [0, \pi]$ using Eqs. (56c) and (58). The orange horizontal line shows $P_{\text{final}} = P_{\text{target}}$. For the H operation, the target final upper energy-level occupation of the qubit $P_{\text{target}} = 1/2$. Larger values of $\mathcal{P}$ provide shorter transition durations and shorter gate durations, so the largest possible value of $\mathcal{P}$ is selected. For the H operation realized with four LZSM transitions, the largest possible value
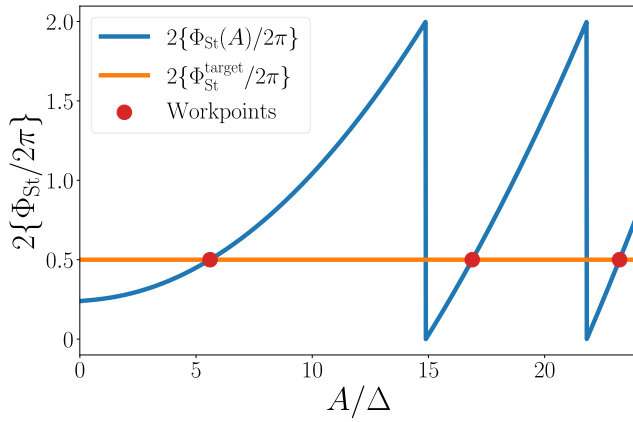
FIG. 6. Graphical procedure of finding possible values of the amplitude A of the drive with four LZSM transitions for the implementation of the Hadamard gate H. The dependence of $2\{\Phi_{St}/2\pi\}$ on the amplitude A of the drive for $\mathcal{P} = \mathcal{P}^*$. Here, Φ_{St} is the Stückelberg phase for the given value of the amplitude A; while Φ_{St}^{target} is the required value of the Stückelberg phase of the drive, found in the previous step, and $\{\}$ is the fractional part. Red dots represent the possible values of the amplitude A of the drive with four LZSM transitions that implement the Hadamard operation H.

$\mathcal{P}^* \approx 0.962$. For the X operation with four LZSM transitions, $\mathcal{P}^* = (2 + \sqrt{2})/4$ coincides with the LZSM transition probability for the H operation, realized with two LZSM transitions, see Eq. (54).

(2) At the second step, we find the Stückelberg phase Φ_{St} that provides the target final transition probability $P_{final} = P_{target}$ given the obtained value of $\mathcal{P}$ using the blue curve in Fig. 5. For the H operation, the solution is given by

$$\Phi_{St} = \frac{\pi}{2} + \pi n, \tag{59}$$

where n is an integer. This is also a condition for the constructive interference between the LZSM transitions.

(3) After finding $\mathcal{P}$ and Φ_{St}, at the third step, we find the amplitude A and frequency ω of the signal (55). Equation (42) defines the relation between the frequency ω and the amplitude A for a certain $\mathcal{P}$. Using Eqs. (42), , (36), (44), and (32), we produce Fig. 6 and find the possible values of the amplitude A of the signal that provides the required value of the Stückelberg phase Φ_{St}^{target}, found in the previous step for the previously found $\mathcal{P} = \mathcal{P}^*$.

(4) Finally, at the fourth step we determine the required idling durations before and after the main part of the drive with LZSM transitions, t_{pre} and t_{after}. Substitution of the obtained evolution matrix of the main part of the drive Ξ_Q to Eq. (57) allows to find the required accumulated phases ϕ_{pre} and ϕ_{after}. Then using Eqs. (13) and (14) we determine the durations t_{pre} and t_{after}. In the example considered here, the accumulated phases $\phi_{pre} = \phi_{after} = \pi/2$, and the durations t_{pre} and t_{after} depend on the choice of the amplitude A in the previous step of the algorithm.

This algorithm of finding the parameters of the drive (55) with an even number of LZSM transitions for the implementation of any single-qubit operation can be summarized as follows.

(1) Find the probability of a single LZSM transition $\mathcal{P}$ which provides the desired final upper-level occupation probability $P_{final} = P_{target}$. See the red curve crossing the orange horizontal line in Fig. 5.

(2) Find the required Stückelberg phase Φ_{St}. See the blue curve in Fig. 5.

(3) Find the combination of the amplitude A and the frequency ω that provides the required values of $\mathcal{P}$ and Φ_{St}. See Fig. 6.

(4) Determine the idling times, t_{pre} and t_{after}, before and after the main part of the drive with LZSM transitions.

This algorithm allows to find the optimal parameters of the drive with an arbitrary even number of LZSM transitions. Here we consider only a two-level quantum system, but real quantum systems are usually multilevel. The LZSM transitions during the passage of nearest level anticrossings with different energy levels will influence the dynamics, so it is important to limit the amplitude of the drive, so that the next nearest anticrossings are not reached.

D. Fidelity

The relaxation and dephasing are not considered in this paper. Thus the infidelities of the gates arise because the theories of RWA and AIM that are used to obtain the parameters of the driving signals are approximate. The infidelities due to numerical solution errors are negligible in comparison with infidelities due to approximations in the theories.

The fidelities are found using quantum tomography [39], which consists in applying the gate for many different initial states, which span the Hilbert space, and then calculating the average fidelity between the obtained states and the target state using [40]

$$F(\rho, \rho_t) = \left(\text{tr}\sqrt{\sqrt{\rho}\rho_t\sqrt{\rho}} \right)^2. \tag{60}$$

Here, ρ is the density matrix obtained by numerical simulation of the qubit dynamics by solving the Liouville-von Neumann equation Eq. (5), and $\rho_t = U\rho_{in}U^\dagger$ is the target state, obtained by applying the gate operator U to the initial density matrix ρ_{in}. Then we calculate the averaged fidelity for different equidistant initial conditions on the Bloch sphere $\bar{F} = \sum_{n=1}^N F(\rho_n, \rho_{t_n})/N$. To better compare the difference between Rabi and LZSM approaches we will use the error rate $D = 1 - \bar{F}$.

The LZSM probability formula $\mathcal{P} = \exp(-2\pi\delta)$ is derived for a linear drive with an infinite time, $\varepsilon(t) = vt$, $t \in (-\infty, \infty)$, leading to an infinite amplitude of the driving signal. Thus, for the considered nonlinear drive $\varepsilon(t) = -A\cos\omega t$ with finite amplitude A, the fidelity of the LZSM gate increases with the amplitude of the drive A. Considering Eq. (42), the amplitude of the drive is proportional to the duration of the gate, $A \sim 1/\omega \sim T$. So the fidelity of the LZSM gate increases with its duration, the gate error D decreases, and a satisfactory balance between the fidelity and speed of the gate should be found. Figure 7 illustrates that the gate error rate D using the LZSM implementation decreases much faster with time than using the usual Rabi approach.

For an arbitrary nonlinear drive, the accuracy of the LZSM formula (35), and thus the fidelity of the gate, increases
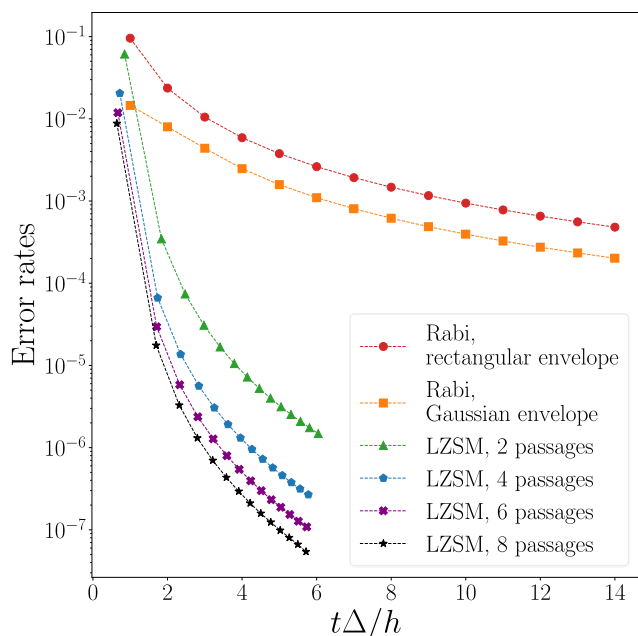
FIG. 7. Comparison of error rates for Rabi and LZSM approaches for single-qubit gate implementations. The error rates $(1 - \bar{F})$ for Rabi and LZSM approaches for single-qubit Y gate implementation calculated for different gate durations $t\Delta/h$. For the Rabi implementation, the gate duration equals an integer number of periods of a resonant driving (from 1 to 14). The Gaussian envelope is cut at $G = 2.7$, see Eq. (27). For the LZSM implementation, the gate durations are built for different workpoints using Fig. 6 and the analogous figures built for higher number of LZSM transitions. Increasing the gate duration, the error for the LZSM approach decreases much faster than for the Rabi approach.

with the linearity of the drive in the anticrossing region, and increases with the distance between the anticrossing region and the starting and final energy detunings ε of the drive.

An alternative method to determine the gates fidelity is Randomized benchmarking [4], which considers how the fidelity decreases with increasing the number of applied operations. Here we only used the quantum tomography method, as a simpler one for numerical calculations.

In experiments, there are methods of improving the gate fidelity based on the back-response loop, also known as quantum control or robust control, for example gradient ascent or Krotov's method [41–44].

IV. TWO-QUBIT GATES

A. Hamiltonian and bases

Now we consider a Hamiltonian of two coupled qubits [1]

$$H = -\frac{1}{2}\sum_{i=1,2}\left(\Delta_i\sigma_x^{(i)} + \varepsilon_i(t)\sigma_z^{(i)}\right) - \frac{g}{4}\left(\sigma_x^{(1)}\sigma_x^{(2)} + \sigma_y^{(1)}\sigma_y^{(2)}\right)$$

$$-\frac{J}{4}\sigma_z^{(1)}\sigma_z^{(2)}, \tag{61}$$

with the external drive of the second qubit which results in the driving $\varepsilon_2(t)$. The energy levels of this Hamiltonian normalized to the coupling strength g are shown in Fig. 8(a).

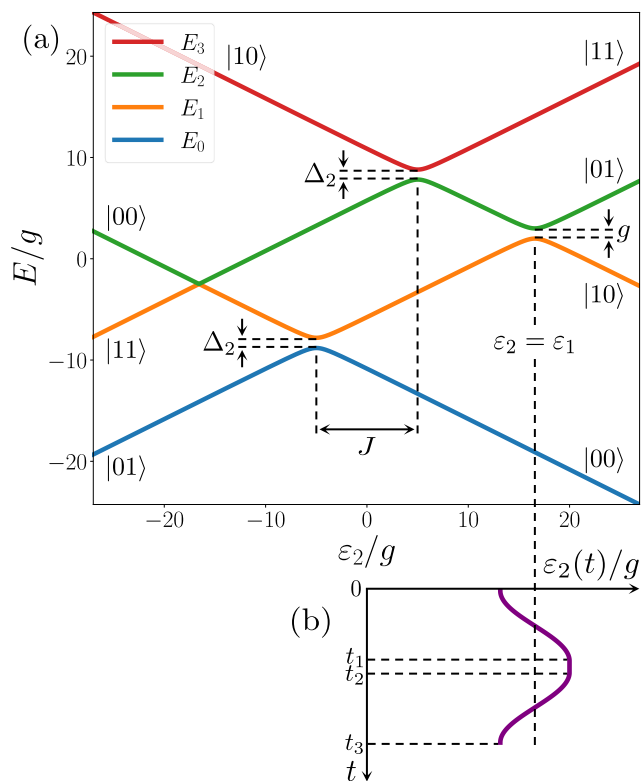

FIG. 8. (a) Adiabatic energy levels of a two-qubit system with Hamiltonian (61) as a function of the driving parameter ε_2. In the regions far from the level anticrossings, the energies of the adiabatic levels $|E_i\rangle$ asymptotically coincide with the energies of the diabatic levels $|mn\rangle$. The parameters of the Hamiltonian used here are: $\Delta_1/g = 0.3$, $\Delta_2/g = 1$, $\varepsilon_1/g = 16.6$, and $J/g = 10$. (b) Time dependence of the driving parameter $\varepsilon_2(t)$ for the iSWAP gate implementation.

Although other choices for the interaction part of the Hamiltonian are possible, we will now consider a transverse coupling with XY interaction

$$H_{\text{int}}^{XY} = -\frac{g}{4}\left(\sigma_x^{(1)}\sigma_x^{(2)} + \sigma_y^{(1)}\sigma_y^{(2)}\right), \tag{62}$$

resulting in a splitting between the E_1 and E_2 adiabatic energy levels versus g at the crossing of the $|01\rangle$ and $|10\rangle$ diabatic energy levels, and longitudial couplings with ZZ-interaction term

$$H_{\text{int}}^{ZZ} = -\frac{J}{4}\sigma_z^{(1)}\sigma_z^{(2)}, \tag{63}$$

resulting in a shift between the $(E_0 - E_1)$ and $(E_2 - E_3)$ adiabatic energy-level anticrossings on the value of J [see Fig. 8(a)]. The JJ or Heisenberg interaction is the particular case when both terms are present and $J = g$.

The difficulty of generating a particular operation depends on the available coupling terms. On the other hand, for each type of coupling there are two-qubit gates which can be implemented in a straightforward manner [45].

The transfer matrix S between the *diabatic* basis $\{|00\rangle, |01\rangle, |10\rangle, |11\rangle\}$ and the *adiabatic* one $\{|E_0\rangle, |E_1\rangle, |E_2\rangle, |E_3\rangle\}$ for the four-level quantum system is constructed as a composition of the eigenvectors of the
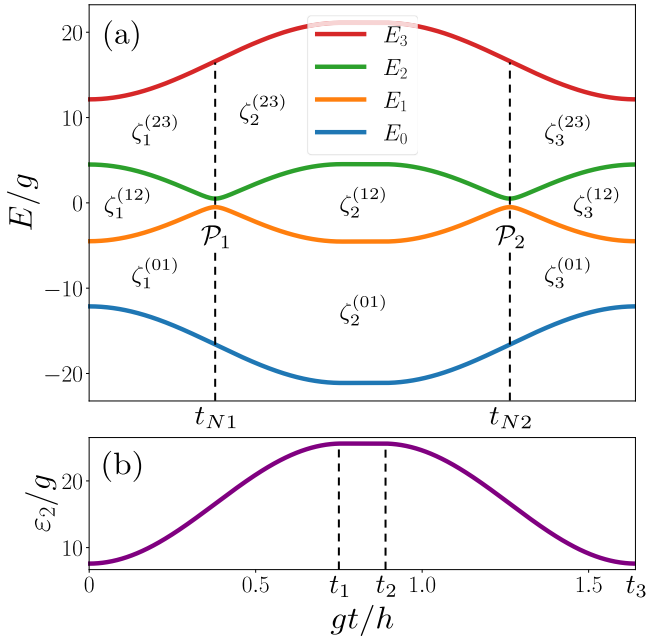
FIG. 9. Dependence of the adiabatic energy levels E_i, (a), and the driving energy detuning ε_2, (b), versus time for the drive (66) for implementing the iSWAP gate. For each diabatic transition N_i during the level anticrossing at time $t_{N(i)}$, the value of the LZSM probability $\mathcal{P}_i$ is introduced. For each adiabatic evolution interval, the phase gains $\zeta_k^{(ij)}$ between various adiabatic levels E_i and E_j can be represented as areas between the levels.

Hamiltonian in the diabatic basis (61), so that the Hamiltonian in the adiabatic basis $H^{(adb)}$ is diagonal with the adiabatic energy levels (the eigenvalues of the Hamiltonian in the diabatic basis) in the ascending order:

$$S^\dagger H S = H^{(adb)} = \text{diag}\{E_0, E_1, E_2, E_3\}. \tag{64}$$

In this section, the transfer matrix S and the adiabatic energy levels E_i are calculated numerically.

B. iSWAP gate

One of the simplest natural two-qubit operations when the XY-type of coupling is present, is an iSWAP gate

$$\text{iSWAP} = \begin{pmatrix} 1 & 0 & 0 & 0 \\ 0 & 0 & i & 0 \\ 0 & i & 0 & 0 \\ 0 & 0 & 0 & 1 \end{pmatrix}. \tag{65}$$

Its LZSM implementation should involve passages of the anticrossing between the adiabatic levels E_1 and E_2, located at $\varepsilon_2 = \varepsilon_1$. For simplicity, here we demonstrate an LZSM realization of the iSWAP gate for the Hamiltonian (61) with only an XY-interaction term, when $J = 0$ and the $(E_0 - E_1)$ and $(E_2 - E_3)$ anticrossings are both located at $\varepsilon_2 = 0$ [see Fig. 8(a)].

As in the case of the X gate, it is impossible to implement an LZSM transition with an arbitrary $\mathcal{P}$ with high fidelity by only one passage, so at least two passages are required. Thus, we consider a drive $\varepsilon_2(t)$ with the following form [see

Figs. 8(b) and 9(b)]:

$$\varepsilon_2(t) = \begin{cases} \varepsilon_1 - A\cos\omega t, & 0 < t < t_1, \\ \varepsilon_1 + A, & t_1 < t < t_2, \\ \varepsilon_1 + A\cos\omega(t - t_2), & t_2 < t < t_3, \end{cases} \tag{66}$$

where

$$t_1 = \frac{T_c}{2}, \quad t_2 = \frac{T_c}{2} + T_1, \quad t_3 = T_c + T_1.$$

It consists of two half-periods of cosine with period $T_c = 2\pi/\omega$ and amplitude A, separated in the middle by an idling period with time T_1. For the simpler form of a signal without the idling, we would obtain a system of three equations on the signal parameters with only two parameters present, A and T_c. So an additional degree of freedom, like an idling time T_1, would be needed.

As in the case of a single qubit, we build the dependence of the adiabatic energy levels on time in Fig. 9(a), introduce all values of the transition probabilities $\mathcal{P}_i$ for each diabatic transition N_i, and define the phase gains $\zeta_k^{(ij)}$ between adiabatic levels E_i and E_j for various periods of the adiabatic evolution as

$$\zeta_k^{(ij)} = \frac{1}{2\hbar} \int_{t_{N(k-1)}}^{t_{N(k)}} [E_j(t) - E_i(t)]dt, \tag{67}$$

where $t_{N0} = 0$, and $t_{N3} = t_3$.

Generally, for a multilevel quantum system, the operator of the *diabatic* (LZSM) transition between the adiabatic energy levels $|E_i\rangle$ and $|E_j\rangle$ ($j = i + 1$) with the LZSM probability $\mathcal{P}$ in the adiabatic basis is defined as

$$N = Re^{i\phi_S}|E_i\rangle\langle E_i| + Re^{-i\phi_S}|E_j\rangle\langle E_j|$$
$$+ \alpha T|E_i\rangle\langle E_j| - \alpha T|E_j\rangle\langle E_i| + \sum_{k\neq i,j}|E_k\rangle\langle E_k|, \tag{68}$$

where the transition and reflection coefficients, T and R, and the Stokes phase ϕ_S are determined by the LZSM probability $\mathcal{P}$, see Eqs. (34) and (36). The sign $\alpha = \pm 1$ depends on the direction of the passage of the adiabatic energy levels anticrossing. Far from the anticrossing region, the energies of the adiabatic states $|E_i\rangle$ and $|E_j\rangle$ asymptotically approach the energies of some diabatic states $|D_m\rangle$ and $|D_n\rangle$, where $m < n$. Here, we assume that the diabatic basis $\{\ldots, |D_m\rangle, \ldots, |D_n\rangle, \ldots\}$ is the one in which the Hamiltonian is defined. If before the passage of the adiabatic energy levels anticrossing the energy of the lower adiabatic level $|E_i\rangle$ is asymptotically close to the energy of the diabatic level with the lower sequence number $|D_m\rangle$, then $\alpha = 1$; if before the passage $|E_i\rangle$ is asymptotically close to $|D_n\rangle$, then $\alpha = -1$.

For the considered Hamiltonian (61), defined in the diabatic basis $\{|00\rangle, |01\rangle, |10\rangle, |11\rangle\}$, and the drive (66), the operators of the diabatic transitions in the adiabatic basis $\{|E_0\rangle, |E_1\rangle, |E_2\rangle, |E_3\rangle\}$ are represented by the matrices

$$N_k = \begin{pmatrix} 1 & 0 & 0 & 0 \\ 0 & R_k e^{i\phi_{S(k)}} & \alpha_k T_k & 0 \\ 0 & -\alpha_k T_k & R_k e^{-i\phi_{S(k)}} & 0 \\ 0 & 0 & 0 & 1 \end{pmatrix}, \tag{69}$$

where $k = 1, 2, \alpha_1 = 1, \alpha_2 = -1$. Here, T_i, R_i, $\phi_{S(i)}$ are the transition, reflection coefficients, and the Stokes phase for the diabatic transition N_i, all determined by the corresponding transition probability $\mathcal{P}_i$ [see Eqs. (34), (35), and (36)].

For an N-level quantum system, the operator of the *adiabatic* evolution in the adiabatic basis is diagonal and given by

$$U = \sum_{k=0}^{N-1} \exp\left\{i\sum_{j=0}^{N-2} \beta_{jk}\zeta^{(j,j+1)}\right\} |E_k\rangle\langle E_k|,$$

$$\beta_{jk} = 2\theta(j-k) - 1, \qquad (70)$$

where $k = 0, 1, \ldots, N-1$, and θ is the Heaviside step function. The rule of the sign $\beta_{jk} = \pm 1$ determination can be summarized as the following: if the area of the phase accumulation, corresponding to the $\zeta^{(j,j+1)}$ term is below the adiabatic energy level E_k, then $\beta_{jk} = -1$; if above it, then $\beta_{jk} = 1$.

For the four-level quantum system, the operator of the adiabatic evolution U_n for the interval of evolution $n = 1, 2, 3$ in the adiabatic basis $\{|E_0\rangle, |E_1\rangle, |E_2\rangle, |E_3\rangle\}$ is represented by a diagonal matrix with the components

$$U_{(n)00} = \exp\left[i\left(\zeta_n^{(01)} + \zeta_n^{(12)} + \zeta_n^{(23)}\right)\right],$$

$$U_{(n)11} = \exp\left[i\left(-\zeta_n^{(01)} + \zeta_n^{(12)} + \zeta_n^{(23)}\right)\right],$$

$$U_{(n)22} = \exp\left[i\left(-\zeta_n^{(01)} - \zeta_n^{(12)} + \zeta_n^{(23)}\right)\right],$$

$$U_{(n)33} = \exp\left[-i\left(\zeta_n^{(01)} + \zeta_n^{(12)} + \zeta_n^{(23)}\right)\right]. \qquad (71)$$

Considering the different order of the basis vectors for the two-level quantum system with $|D_0\rangle = |1\rangle$ and $|D_1\rangle = |0\rangle$ (see Sec. II), the operators of the diabatic transition (68) and adiabatic evolution (70) are also consistent with the matrices of the diabatic transitions (33), (38) and adiabatic evolution (31) for a single qubit.

The evolution matrix for the whole drive becomes

$$\Xi = U_3 N_2 U_2 N_1 U_1. \qquad (72)$$

After simplifying by

$$\zeta^{(01)} = \zeta_1^{(01)} + \zeta_2^{(01)} + \zeta_3^{(01)}, \quad \zeta^{(23)} = \zeta_1^{(23)} + \zeta_2^{(23)} + \zeta_3^{(23)}, \qquad (73)$$

taking the common phase $e^{i\varphi}$ out of the matrix and neglecting it [see Eq. (12)], we obtain the evolution matrix

$$\Xi = \begin{pmatrix} 1 & 0 & 0 & 0 \\ 0 & u_{11} & u_{12} & 0 \\ 0 & u_{21} & u_{22} & 0 \\ 0 & 0 & 0 & e^{i\phi_3} \end{pmatrix}, \qquad (74)$$

that depends on the values $\mathcal{P}_1, \mathcal{P}_2, \zeta^{(01)}, \zeta_i^{(12)}, \zeta^{(23)}$. Equating it to the matrix of a required two-qubit iSWAP gate allows to determine the parameters of the external drive which implement this gate:

$$\mathcal{P}_1 + \mathcal{P}_2 = 1,$$

$$\phi_{S1} + \phi_{S2} + 2\zeta_2^{(12)} = \pi + 2\pi n_1,$$

$$\phi_{S1} + 2\left(\zeta^{(01)} + \zeta_1^{(12)} + \zeta_2^{(12)}\right) = \frac{\pi}{2} + 2\pi n_2,$$

$$\phi_{S2} + 2\left(\zeta^{(01)} + \zeta_2^{(12)} + \zeta_3^{(12)}\right) = \frac{\pi}{2} + 2\pi n_3. \qquad (75)$$
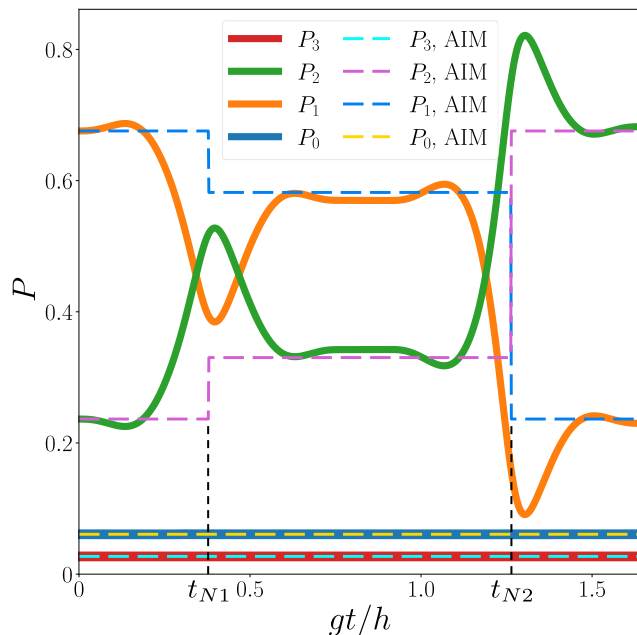

FIG. 10. The dynamics of the iSWAP gate implemented with two LZSM transitions. The occupation probabilities P_i of each adiabatic level E_i as function of time are obtained by two methods: the numerical solution of the Liouville-von Neumann equation, shown by solid lines, and by the adiabatic-impulse model, indicated by dashed lines. The final occupation probabilities, found by the adiabatic-impulse model, represent the expected occupation probabilities of the gate. The iSWAP gate results in the swap of occupation probabilities between the E_1 and E_2 adiabatic energy levels.

For the considered signal (66) with $\mathcal{P}_1 = \mathcal{P}_2 = \mathcal{P}$, resulting in $\zeta_1^{(12)} = \zeta_3^{(12)}$, and in the case when only the XY-interaction is present ($J = 0$), resulting in $\zeta^{(01)} = \zeta^{(23)}$, the conditions simplify to

$$\mathcal{P} = \frac{1}{2},$$

$$\phi_S + \zeta_2^{(12)} = \frac{\pi}{2} + \pi n_1,$$

$$\phi_S + 2\left(\zeta^{(01)} + \zeta_1^{(12)} + \zeta_2^{(12)}\right) = \frac{\pi}{2} + 2\pi n_2. \qquad (76)$$

The first equation results in a linear dependence between A and T_c:

$$A = \frac{g^2}{4\hbar \ln 2} T_c. \qquad (77)$$

Then we numerically solve two other equations on two parameters of the signal T_c and T_1. In Fig. 10, we show the dynamics of the iSWAP gate for a particular solution with $gT_c/h = 1.517$, $gT_1/h = 0.125$, and $A/g = 3.438$ for the Hamiltonian (61), with the parameters $\Delta_1/g = 0.3$, $\Delta_2/g = 1$, $\varepsilon_1/g = 16.6$, $J = 0$; and compare the approximate solution obtained by the adiabatic-impulse model with the numerical solution of the Schrödinger equation. The same parameters of the Hamiltonian and drive were used for Fig. 9, with the exception of the larger amplitude $A/g = 9$.

The fidelity criteria for a single-qubit gate, described in Sec. III D can be extended on the multilevel quantum systems with several energy level anticrossings. Firstly, the fidelity

of the gate increases with the linearity of the external drive $\varepsilon_i(t)$ of the ith qubit in all regions of the adiabatic level anticrossings, which are passed during the driving. Secondly, it increases with distance increase between both starting and final energy detunings ε_i to the nearest passed energy level anticrossing region, given that the starting and final energy detunings are still far from the other nonpassed anticrossings. The detailed conditions depend on the exact time dependence $\varepsilon_i(t)$ of the drive. For the considered signal (66), the fidelity of the iSWAP gate increases with the amplitude of the signal A, as long as the starting and final detunings ε_2 are not close to the region of the E_2 and E_3 levels anticrossing (see Fig. 8).

Considering Eq. (77), the duration of the gate also increases with the increase of amplitude of the drive A, so as in the single-qubit case, the fidelity of the iSWAP gate increases with its duration, and a satisfactory balance between the fidelity and speed of the gate should be found.

Note that the system of equations for implementing a required single- or two-qubit gate [e.g., Eqs. (46), (50), (54), (75), and (76), the systems of equations for other two-qubit gates in Appendices A and B] does not depend on the specific analytical definition of the external drive $\varepsilon_2(t)$ [e.g., Eq. (66)] and is valid for any drive with a similar shape, which has the identical combination of passages of the adiabatic level anticrossings, providing a topologically similar time dependence of the adiabatic energy levels (see, e.g., Fig. 9).

Generally, for an N-level quantum system, if the quantum logic gates are considered in the *adiabatic* basis, the drive with the passages of the anticrossing of the adiabatic energy levels E_i and E_j (where $j = i + 1$) allows to implement the gates with the generalized matrix

$$\Xi = u_{ii}|E_i\rangle\langle E_i| + u_{ij}|E_i\rangle\langle E_j| + u_{ji}|E_j\rangle\langle E_i|$$
$$+ u_{jj}|E_j\rangle\langle E_j| + \sum_{k \neq i,j} e^{i\phi_k}|E_k\rangle\langle E_k|$$

$$= \begin{pmatrix} e^{i\phi_0} & 0 & \dots & \dots & \dots & 0 \\ 0 & \ddots & & & & \vdots \\ \vdots & & u_{ii} & u_{ij} & & \vdots \\ \vdots & & u_{ji} & u_{jj} & & \vdots \\ \vdots & & & & \ddots & 0 \\ 0 & \dots & \dots & \dots & 0 & e^{i\phi_{N-1}} \end{pmatrix}, \quad (78)$$

which represents the evolution operator for this drive in the *adiabatic* basis.

V. CONCLUSIONS

We further developed the paradigm of alternative quantum logic gates, based on LZSM transitions. We demonstrated how the adiabatic-impulse model can be used for implementing single- and two-qubit quantum logic gates, in particular X, Y, Hadamard, iSWAP and CNOT gates, demonstrated how to increase the gate speed, and the technique of finding the trade-off and balance between speed and fidelity of the gates. We also demonstrated the comparison of the theoretical error rate for conventional Rabi-based gates and alternative LZSM gates for various logic gate durations.

The adiabatic-impulse model is applicable for any quantum multilevel systems with two conditions. Firstly, it works well for a large drive amplitude, $A > \Delta$. In terms of the requirements for a quantum system, this means that for the considered level anticrossing, its minimal energy splitting Δ should be much less than the distance to the nearest level anticrossings. Secondly, the time between the LZSM transitions should be larger than the time needed for the transition process. This condition limits the maximal frequency of the driving signal in the multipassage implementation, and the minimal gate duration, respectively.

An arbitrary single-qubit quantum logic gate can be performed with only two LZSM transitions. However, the considered option of gate implementation with multiple LZSM transitions provide a better combination of gate duration and fidelity. We demonstrated the technique of implementing an arbitrary single-qubit quantum logic gate with an arbitrary number of LZSM transitions.

The considered general method of implementing quantum logic gates with LZSM transitions using the adiabatic-impulse model is applicable to a large variety of multilevel quantum systems. This method is the following: choose the shape of the driving signal so that it passes the required level anticrossings for a given gate. For the considered signal compute the dependence of the adiabatic energy levels of the system on time. Introduce the transition probabilities $\mathcal{P}_i$ for each diabatic transition and phase gains $\zeta_k^{(ij)}$ between all pairs of successive adiabatic levels E_i and E_j for each period of adiabatic evolution. Using them, compose all matrices of the diabatic transition N_i and adiabatic evolution U_i, multiply them, and obtain the total evolution matrix. Equating it to the matrix of the required quantum logic gate multiplied by an arbitrary phase term $e^{i\varphi}$ allows to determine the required parameters of the driving signal, that implements this logic gate.

APPENDIX A: GENERALIZED SWAP GATES

The passages of the anticrossing between the adiabatic energy levels E_1 and E_2 at $\varepsilon_2 = \varepsilon_1$ [see Fig. 8(a)] allow to implement generalized two-qubit swap gates with the matrix (74), including the SWAP, $\sqrt{\text{SWAP}}$, $\sqrt{\text{iSWAP}}$, SWAP$^\alpha$, fermionic simulation $U_{\text{fSim}}(\theta, \phi)$ gates, etc. In this Appendix, the variables $\mathcal{P}_i$, $\phi_{\text{S}(i)}$, $\zeta_k^{(ij)}$ refer to Sec. IV B and Fig. 9(a).

1. SWAP and iSWAP gates

The system of equations (75) written for the SWAP gate is not compatible. Thus, the SWAP gate cannot be implemented by only two passages of the $(E_1 - E_2)$ adiabatic energy-level anticrossing for the Hamiltonian (61) with only XY coupling. It can, however, be implemented when $\zeta^{(01)} \neq \zeta^{(23)}$, in case both XY and ZZ interactions are present, as in Fig. 8(a). The corresponding conditions are written as

$$\mathcal{P}_1 + \mathcal{P}_2 = 1,$$

$$\phi_{S1} + \phi_{S2} + 2\zeta_2^{(12)} = \pi + 2\pi n_1,$$

$$\phi_{S1} + 2\big(\zeta^{(01)} + \zeta_1^{(12)} + \zeta_2^{(12)}\big) = (1 + \lambda)\frac{\pi}{2} + 2\pi n_2,$$

$$\phi_{S2} + 2\big(\zeta^{(01)} + \zeta_2^{(12)} + \zeta_3^{(12)}\big) = (1 + \lambda)\frac{\pi}{2} + 2\pi n_3,$$

$$\zeta^{(01)} + \zeta_1^{(12)} + \zeta_2^{(12)} + \zeta_3^{(12)} + \zeta^{(23)} = \pi n_4, \tag{A1}$$

where $\lambda = 1$ for the SWAP gate and $\lambda = 0$ for the iSWAP gate.

2. $\sqrt{\text{SWAP}}$ and $\sqrt{\text{iSWAP}}$ gates

The $\sqrt{\text{SWAP}}$ and $\sqrt{\text{iSWAP}}$ gates do not provide a full swap of the occupation probabilities between the adiabatic energy levels E_1 and E_2 when $\mathcal{P} = 1$; so they could be also implemented by a single passage of the $(E_1 - E_2)$ level anticrossing. For the simplest drive $\varepsilon_2(t)$ with only one passage of the $(E_1 - E_2)$ level anticrossing at $\varepsilon_2 = \varepsilon_1$ [see Fig. 8(a)] in the direction of the energy detuning ε_2 increase, the evolution matrix is given by

$$\Xi = U_2 N_1 U_1, \tag{A2}$$

where the diabatic transition N_1 and adiabatic evolution U_k matrices are defined by (69) and (71). After the simplification (73), taking the common phase $e^{i\varphi}$ out of the matrix and neglecting it [see Eq. (12)], equating the evolution matrix to the matrix of the required quantum logic gate provide the conditions for the drive, which implement this gate:

$$\mathcal{P}_1 = \frac{1}{2},$$

$$\zeta_1^{(01)} + \zeta_2^{(01)} = -\frac{1 + \lambda}{2}\frac{\pi}{8} + \frac{\phi_{S1}}{2} + \pi n_1,$$

$$\zeta_1^{(12)} = \lambda\frac{\pi}{4} - \frac{\phi_{S1}}{2} + \pi n_2,$$

$$\zeta_2^{(12)} = -\lambda\frac{\pi}{4} - \frac{\phi_{S1}}{2} + \pi n_3,$$

$$\zeta_1^{(23)} + \zeta_2^{(23)} = \frac{\phi_{S1}}{2} + \pi n_4, \tag{A3}$$

where $\lambda = 1$ for the $\sqrt{\text{SWAP}}$ gate and $\lambda = -1$ for the $\sqrt{\text{iSWAP}}$ gate.

APPENDIX B: GENERALIZED CONTROLLED-U GATES

When the ZZ coupling is present, the passages of the anticrossing between adiabatic energy levels E_2 and E_3 at $\varepsilon_2 = J/2$ [see Fig. 8(a)] allow to implement two-qubit gates
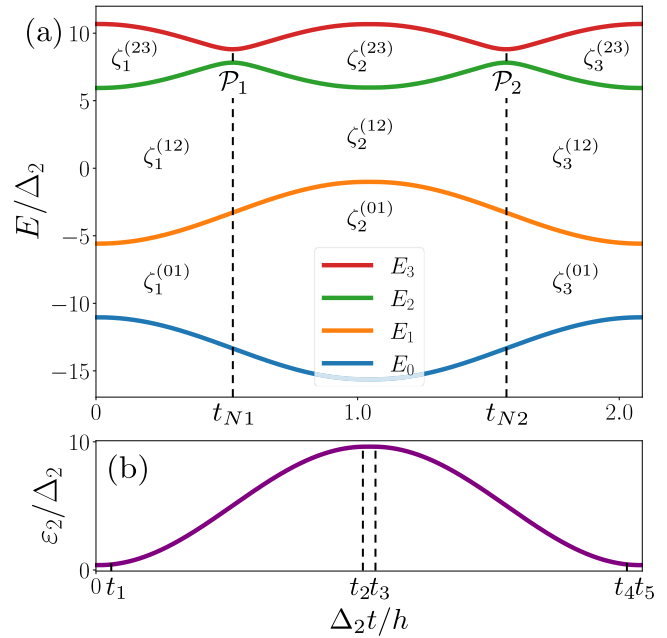

FIG. 11. Dependence of the adiabatic energy levels E_i, (a), and the driving parameter, energy detuning ε_2, (b), versus time for the drive (B2) for implementing the CNOT gate. For each diabatic transition N_i during the level anticrossing at time $t_{N(i)}$, the value of the LZSM probability $\mathcal{P}_i$ is introduced. For each adiabatic evolution interval, the phase gains $\zeta_k^{(ij)}$ between various adiabatic levels E_i and E_j, represented as areas between the levels.

with the matrix

$$\Xi = \begin{pmatrix} 1 & 0 & 0 & 0 \\ 0 & e^{i\phi_1} & 0 & 0 \\ 0 & 0 & u_{22} & u_{23} \\ 0 & 0 & u_{32} & u_{33} \end{pmatrix}, \tag{B1}$$

in particular the controlled-U gates when $u_{11} = e^{i\phi_1} = 1$. These include the CNOT, CPhase(ϕ), CZ, CS gates, etc.

1. CNOT gate

Here we demonstrate an LZSM realization of the CNOT gate for the Hamiltonian (61) with both XY and ZZ couplings, although only ZZ is required. As for the X gate, it is impossible to implement an LZSM transition with an arbitrary $\mathcal{P}$ with high fidelity by only one passage; so at least two passages are required. We now consider a drive $\varepsilon_2(t)$ in the following form [see Fig. 11(b)]:

$$\varepsilon_2(t) = \begin{cases} J/2 - A, & 0 < t < t_1, \\ J/2 - A\cos\omega(t - t_1), & t_1 < t < t_2, \\ J/2 + A, & t_2 < t < t_3, \\ J/2 + A\cos\omega(t - t_3), & t_3 < t < t_4, \\ J/2 - A, & t_4 < t < t_5, \end{cases} \tag{B2}$$

where

$$t_1 = T_1, \quad t_2 = T_1 + \frac{T_c}{2}, \quad t_3 = T_1 + \frac{T_c}{2} + T_2,$$

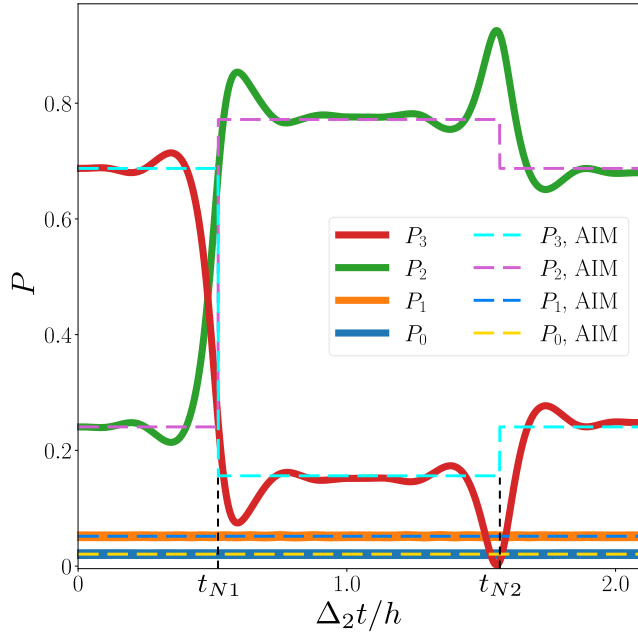$$t_4 = T_1 + T_c + T_2, \quad t_5 = 2T_1 + T_c + T_2.$$

FIG. 12. The dynamics of the CNOT gate implemented with two LZSM transitions. The occupation probabilities P_i of each adiabatic level E_i as function of time are obtained by two methods: the numerical solution of the Liouville-von Neumann equation, shown by solid lines, and by the adiabatic-impulse model, shown by dashed lines. The final occupation probabilities, found by the adiabtic-impulse model, represent the expected occupation probabilities of the gate. The CNOT gate results in the swap of occupation probabilities between the E_2 and E_3 adiabatic energy levels.

As in the case of the single-qubit and iSWAP gates, we compute the time dependence of the adiabatic energy levels [see Fig. 11(a)], introduce the values of the transition probabilities $\mathcal{P}_i$ for each diabatic transition N_i, and define all phase gains $\zeta_k^{(ij)}$ (67) between adiabatic levels E_i and E_j for the various periods of the adiabatic evolution.

The operators of the *diabatic* transitions (68) are represented b y the matrices

$$N_k = \begin{pmatrix} 1 & 0 & 0 & 0 \\ 0 & 1 & 0 & 0 \\ 0 & 0 & R_k e^{i\phi_{\mathrm{Sk}}} & -\alpha_k T_k \\ 0 & 0 & \alpha_k T_k & R_k e^{-i\phi_{\mathrm{Sk}}} \end{pmatrix}, \qquad (B3)$$

where $k = 1, 2, \alpha_1 = 1, \alpha_2 = -1$. The matrix of the *adiabatic* evolution is given by Eq. (71). The evolution matrix for the whole drive can be found as (72). After simplifying by

$$\zeta^{(01)} = \zeta_1^{(01)} + \zeta_2^{(01)} + \zeta_3^{(01)}, \quad \zeta^{(12)} = \zeta_1^{(12)} + \zeta_2^{(12)} + \zeta_3^{(12)}, \tag{B4}$$

taking the common phase $e^{i\varphi}$ out of the matrix and neglecting it [see Eq. (12)], we obtain the evolution matrix in the form (B1), which depends on the values $\mathcal{P}_1$, $\mathcal{P}_2$, $\zeta^{(01)}$, $\zeta^{(02)}$, $\zeta_i^{(23)}$. Equating it to the matrix of a required two-qubit

CNOT gate

$$\mathrm{CNOT} = \begin{pmatrix} 1 & 0 & 0 & 0 \\ 0 & 1 & 0 & 0 \\ 0 & 0 & 0 & 1 \\ 0 & 0 & 1 & 0 \end{pmatrix} \tag{B5}$$

allows to determine the parameters of the external drive which implement this gate:

$$\mathcal{P}_1 + \mathcal{P}_2 = 1,$$

$$\zeta^{(01)} = \pi n_1,$$

$$\phi_{\mathrm{S}1} + \phi_{\mathrm{S}2} + 2\zeta_2^{(23)} = \pi + 2\pi n_2,$$

$$\phi_{\mathrm{S}1} + 2\zeta^{(12)} + 2\zeta_1^{(23)} + 2\zeta_2^{(23)} = 2\pi n_3,$$

$$\phi_{\mathrm{S}2} + 2\zeta^{(12)} + 2\zeta_2^{(23)} + 2\zeta_3^{(23)} = 2\pi n_4. \tag{B6}$$

For the considered signal (B2) with $\mathcal{P}_1 = \mathcal{P}_2 = \mathcal{P}$ and $\zeta_1^{(23)} = \zeta_3^{(23)}$, the conditions simplify to

$$\mathcal{P} = \frac{1}{2},$$

$$\zeta^{(01)} = \pi n_1,$$

$$\phi_{\mathrm{S}} + \zeta_2^{(23)} = \frac{\pi}{2} + \pi n_2,$$

$$\phi_{\mathrm{S}} + 2\zeta^{(12)} + 2\zeta_1^{(23)} + 2\zeta_2^{(23)} = 2\pi n_3. \tag{B7}$$

In Fig. 12, we illustrate the dynamics of the CNOT gate for a particular solution with $\Delta_2 T_c/h = 2.0394$, $\Delta_2 T_1/h = 0.0109$, $\Delta_2 T_2/h = 0.0288$, $A/\Delta_2 = 4.6217$ for the Hamiltonian (61) with the parameters $\Delta_1/g = 0.3$, $\Delta_2/g = 1$, $\varepsilon_1/g = 16.6$, $J/g = 10$, and compare the approximate solution obtained by the adiabatic-impulse model with the numerical solution of the Liouville-von Neumann equation. The same parameters of the Hamiltonian and drive were used for Fig. 11.

2. CPhase(ϕ), CZ, CS gates

Equating the evolution matrix (B1) for the external drive $\varepsilon_2(t)$ with the shape (B2) to the matrix of the CPhase(ϕ) gate

$$\mathrm{CPhase}(\phi) = \begin{pmatrix} 1 & 0 & 0 & 0 \\ 0 & 1 & 0 & 0 \\ 0 & 0 & 1 & 0 \\ 0 & 0 & 0 & e^{i\phi} \end{pmatrix} \tag{B8}$$

provides the conditions for the external drive which implements this gate:

$$\mathcal{P}_1 = \mathcal{P}_2 = \mathcal{P},$$

$$\zeta^{(01)} = \pi n_1,$$

$$\phi_{\mathrm{S}} + \zeta_2^{(23)} = \pi n_2,$$

$$\zeta^{(12)} + \zeta_2^{(23)} = \pi n_3$$

$$\zeta^{(12)} + \zeta_1^{(23)} + \zeta_3^{(23)} = -\frac{\phi}{2} + \pi n_4. \tag{B9}$$

Here, the variables $\mathcal{P}_i$, ϕ_{S}, $\zeta_k^{(ij)}$ refer to Appendix B1 and Fig. 11(a). The particular cases of the CPhase(ϕ) gate are the CZ ($\phi = \pi$) and CS ($\phi = \pi/2$) gates.

[1] P. Krantz, M. Kjaergaard, F. Yan, T. P. Orlando, S. Gustavsson, and W. D. Oliver, A quantum engineer's guide to superconducting qubits, Appl. Phys. Rev. **6**, 021318 (2019).

[2] X. Gu, A. F. Kockum, A. Miranowicz, Y.-X. Liu, and F. Nori, Microwave photonics with superconducting quantum circuits, Phys. Rep. **718-719**, 1 (2017).

[3] A. F. Kockum, A. Miranowicz, S. D. Liberato, S. Savasta, and F. Nori, Ultrastrong coupling between light and matter, Nat. Rev. Phys. **1**, 19 (2019).

[4] T. Jones, K. Steven, X. Poncini, M. Rose, and A. Fedorov, Approximations in transmon simulation, Phys. Rev. Appl. **16**, 054039 (2021).

[5] Y.-C. Yang, S. N. Coppersmith, and M. Friesen, Achieving high-fidelity single-qubit gates in a strongly driven silicon-quantum-dot hybrid qubit, Phys. Rev. A **95**, 062321 (2017).

[6] D. L. Campbell, Y.-P. Shim, B. Kannan, R. Winik, D. K. Kim, A. Melville, B. M. Niedzielski, J. L. Yoder, C. Tahan, S. Gustavsson, and W. D. Oliver, Universal nonadiabatic control of small-gap superconducting qubits, Phys. Rev. X **10**, 041051 (2020).

[7] S. N. Shevchenko, S. Ashhab, and F. Nori, Landau–Zener–Stückelberg interferometry, Phys. Rep. **492**, 1 (2010).

[8] O. V. Ivakhnenko, S. N. Shevchenko, and F. Nori, Nonadiabatic Landau–Zener–Stückelberg–Majorana transitions, dynamics, and interference, Phys. Rep. **995**, 1 (2023).

[9] J. He, D. Pan, M. Liu, Z. Lyu, Z. Jia, G. Yang, S. Zhu, G. Liu, J. Shen, S. N. Shevchenko, F. Nori, J. Zhao, L. Lu, and F. Qu, Quantifying quantum coherence of multiple-charge states in tunable Josephson junctions, npj Quantum Inf. **10**, 1 (2024).

[10] E. P. Glasbrenner and W. P. Schleich, The Landau-Zener formula made simple, J. Phys. B: At. Mol. Opt. Phys. **56**, 104001 (2023).

[11] T. Weitz, C. Heide, and P. Hommelhoff, Strong-field Bloch electron interferometry for band-structure retrieval, Phys. Rev. Lett. **132**, 206901 (2024).

[12] J. G. Russo and M. Tierz, Landau-Zener transition rates of superconducting qubits and the absorption spectrum in quantum dots, Phys. Rev. A **109**, 033702 (2024).

[13] M.-Y. Chen, C. Zhang, and Z.-Y. Xue, Fast high-fidelity geometric gates for singlet-triplet qubits, Phys. Rev. A **105**, 022620 (2022).

[14] S. Kwon, A. Tomonaga, G. L. Bhai, S. J. Devitt, and J.-S. Tsai, Gate-based superconducting quantum computing, J. Appl. Phys. **129**, 041102 (2021).

[15] A. F. Kockum and F. Nori, Quantum bits with Josephson junctions, in *Fundamentals and Frontiers of the Josephson Effect*, edited by F. Tafuri, Springer Series in Materials Science, Vol. 286 (Springer, Cham, 2019), pp. 703–741.

[16] C. M. Quintana, K. D. Petersson, L. W. McFaul, S. J. Srinivasan, A. A. Houck, and J. R. Petta, Cavity-mediated entanglement generation via Landau-Zener interferometry, Phys. Rev. Lett. **110**, 173603 (2013).

[17] Z. Li, D. Li, M. Li, X. Yang, S. Song, Z. Han, Z. Yang, J. Chu, X. Tan, D. Lan, H. Yu, and Y. Yu, Quantum state transfer via multi-passage Landau–Zener–Stückelberg interferometry in a three-qubit system, Phys. Status Solidi B **257**, 1900459 (2020).

[18] Z.-T. Zhang and Y. Yu, Processing quantum information in a hybrid topological qubit and superconducting flux qubit system, Phys. Rev. A **87**, 032327 (2013).

[19] A. Migliore and A. Messina, Controlling the charge-transfer dynamics of two-level systems around avoided crossings, J. Chem. Phys. **160**, 084112 (2024).

[20] V. Benza and G. Strini, A single qubit Landau-Zener gate, Fortschr. Phys. **51**, 14 (2003).

[21] C. Hicke, L. F. Santos, and M. I. Dykman, Fault-tolerant Landau-Zener quantum gates, Phys. Rev. A **73**, 012342 (2006).

[22] L. F. Wei, J. R. Johansson, L. X. Cen, S. Ashhab, and F. Nori, Controllable coherent population transfers in superconducting qubits for quantum computing, Phys. Rev. Lett. **100**, 113601 (2008).

[23] J. J. Cáceres, D. Domínguez, and M. J. Sánchez, Fast quantum gates based on Landau-Zener-Stückelberg-Majorana transitions, Phys. Rev. A **108**, 052619 (2023).

[24] G. Cao, H.-O. Li, T. Tu, L. Wang, C. Zhou, M. Xiao, G.-C. Guo, H.-W. Jiang, and G.-P. Guo, Ultrafast universal quantum control of a quantum-dot charge qubit using Landau–Zener–Stückelberg interference, Nat. Commun. **4**, 1401 (2013).

[25] L. Wang, T. Tu, B. Gong, C. Zhou, and G.-C. Guo, Experimental realization of non-adiabatic universal quantum gates using geometric Landau-Zener-Stückelberg interferometry, Sci. Rep. **6**, 19048 (2016).

[26] H. Zhang, S. Chakram, T. Roy, N. Earnest, Y. Lu, Z. Huang, D. K. Weiss, J. Koch, and D. I. Schuster, Universal fast-flux control of a coherent, low-frequency qubit, Phys. Rev. X **11**, 011010 (2021).

[27] K. M. Abadir, Expansions for some confluent hypergeometric functions, J. Phys. A: Math. Gen. **26**, 4059 (1993).

[28] C. Heide, T. Boolakee, T. Higuchi, H. B. Weber, and P. Hommelhoff, Interaction of carrier envelope phase-stable laser pulses with graphene: The transition from the weak-field to the strong-field regime, New J. Phys. **21**, 045003 (2019).

[29] C. Heide, T. Boolakee, T. Higuchi, and P. Hommelhoff, Sub-cycle temporal evolution of light-induced electron dynamics in hexagonal 2D materials, J. Phys. Phot. **2**, 024004 (2020).

[30] C. Heide, T. Boolakee, T. Higuchi, and P. Hommelhoff, Adiabaticity parameters for the categorization of light-matter interaction: From weak to strong driving, Phys. Rev. A **104**, 023103 (2021).

[31] S. Cong, M.-Y. Gao, G. Cao, G.-C. Guo, and G.-P. Guo, Ultrafast manipulation of a double quantum-dot charge qubit using Lyapunov-based control method, IEEE J. Quantum Electron. **51**, 1 (2015).

[32] J. R. Johansson, P. D. Nation, and F. Nori, QuTiP: An open-source Python framework for the dynamics of open quantum systems, Comput. Phys. Commun. **183**, 1760 (2012).

[33] J. R. Johansson, P. D. Nation, and F. Nori, QuTiP 2: A Python framework for the dynamics of open quantum systems, Comput. Phys. Commun. **184**, 1234 (2013).

[34] P. Kaye, R. Laflamme, and M. Mosca, *An Introduction to Quantum Computing* (Oxford University Press, New York, 2006).

[35] S. Ashhab, J. R. Johansson, A. M. Zagoskin, and F. Nori, Two-level systems driven by large-amplitude fields, Phys. Rev. A **75**, 063414 (2007).

[36] N. V. Vitanov and K. A. Suominen, Nonlinear level-crossing models, Phys. Rev. A **59**, 4580 (1999).

[37] M. Sillanpää, T. Lehtinen, A. Paila, Y. Makhlin, and P. Hakonen, Continuous-time monitoring of Landau-Zener interference in a Cooper-pair box, Phys. Rev. Lett. **96**, 187002 (2006).

[38] M. Sillanpää, T. Lehtinen, A. Paila, Y. Makhlin, and P. J. Hakonen, Landau–Zener interferometry in a Cooper-pair box, J. Low Temp. Phys. **146**, 253 (2007).

[39] N. V. Vitanov, Relations between single and repeated qubit gates: coherent error amplification for high-fidelity quantum-gate tomography, New J. Phys. **22**, 023015 (2020).

[40] R. Jozsa, Fidelity for mixed quantum states, J. Mod. Opt. **41**, 2315 (1994).

[41] M. Kuzmanović, I. Björkman, J. J. McCord, S. Dogra, and G. S. Paraoanu, High-fidelity robust qubit control by phase-modulated pulses, Phys. Rev. Res. **6**, 013188 (2024).

[42] T. Araki, F. Nori, and C. Gneiting, Robust quantum control with disorder-dressed evolution, Phys. Rev. A **107**, 032609 (2023).

[43] S.-Y. Huang and H.-S. Goan, Optimal control for fast and high-fidelity quantum gates in coupled superconducting flux qubits, Phys. Rev. A **90**, 012318 (2014).

[44] B. Li, S. Ahmed, S. Saraogi, N. Lambert, F. Nori, A. Pitchford, and N. Shammah, Pulse-level noisy quantum circuits with QuTiP, Quantum **6**, 630 (2022).

[45] N. Schuch and J. Siewert, Natural two-qubit gate for quantum computation using the XY interaction, Phys. Rev. A **67**, 032301 (2003).